The apo -form of the Vibrio cholerae replicative helicase DnaB is a labile and inactive planar trimer of dimers

Claire Cargemel, Hélène Walbott, Dominique Durand, Pierre Legrand, Malika Ouldali, Jean-luc Ferat, Stéphanie Marsin, Sophie Quevillon-Cheruel

FEBS Letters

FEBS PRESS science publishing by scientists

RESEARCH LETTER

The *apo*-form of the *Vibrio cholerae* replicative helicase DnaB is a labile and inactive planar trimer of dimers

Claire Cargemel[1], Hélène Walbott[1], Dominique Durand[1], Pierre Legrand[2], Malika Ouldali[1], Jean-Luc Ferat[1], Stéphanie Marsin[1] and Sophie Quevillon-Cheruel[1]

1 CEA, CNRS, Institute for Integrative Biology of the Cell (I2BC), Université Paris-Saclay, Gif-sur-Yvette, France
2 Synchrotron SOLEIL, Gif-sur-Yvette, France

Correspondence
S. Quevillon-Cheruel, CEA, CNRS, Institute for Integrative Biology of the Cell (I2BC), Université Paris-Saclay, Gif-sur-Yvette 91198, France
Tel: +33 1 69826115
E-mail: sophie.quevillon-cheruel@i2bc.paris-saclay.fr

Claire Cargemel and Hélène Walbott contributed equally to this article

(Received 5 April 2022, revised 5 May 2022, accepted 9 May 2022, available online 23 May 2022)

doi:10.1002/1873-3468.14403

Edited by Marina Mapelli

To enable chromosomal replication, DNA is unwound by the ATPase molecular motor replicative helicase. The bacterial helicase DnaB is a ring-shaped homo-hexamer whose conformational dynamics are being studied through its different 3D structural states adopted along its functional cycle. Our findings describe a new crystal structure for the *apo*-DnaB from *Vibrio cholerae*, forming a planar hexamer with *pseudo*-symmetry, constituted by a trimer of dimers in which the C-terminal domains delimit a triskelion-shaped hole. This hexamer is labile and inactive. We suggest that it represents an intermediate state allowing the formation of the active NTP-bound hexamer from dimers.

Keywords: replicative helicase; X-ray structure

Efficient and accurate replication of chromosomal DNA is an essential process, observed in all cells, which ensures faithful cell division. In bacteria, DNA replication usually starts at a single origin to proceed bidirectionally until it reaches a defined terminal region, and is carried out by the replisome, a complex macromolecular machinery. The architecture and dynamics of bacterial replisomes have been extensively characterized [1,2]. They are composed of several proteins, the PolIII polymerase complex, the DnaG primase, the clamp loader, the SSB protein and the DnaB helicase, which work together to coordinate DNA unwinding and leading- and lagging-strands synthesis [3].

The bacterial DnaB replicative helicase, powered by the energy released by NTP hydrolysis, is the molecular motor that unwinds double-stranded DNA in front of the replication forks, resulting in the separation of the duplex DNA into single strands. Recall that DnaB belongs to the helicase superfamily 4 (SF4) and translocates on the lagging strand in the 5′ → 3′ direction [4,5]. The active protein is a toroid homo-hexamer [6–8], and each monomer is composed of two structural domains. The N-terminal domain (NTD) is composed of a helical globular head supplemented by two hairpin helices, while the C-terminal domain (CTD) is a RecA-core domain that belongs to the additional strand catalytic glutamate (ASCE) class of P-loop NTPases [7,9]. The NTD and the CTD are connected through a linker containing an α-helix [7]. Within the helicase hexamers, adjacent NTDs interact pairwise through coiled-coil contacts to form

Abbreviations
CTD, C-terminal domain; DH, determinant helix; LH, linker helix; NTD, N-terminal domain; SAXS, small-angle X-ray scattering; SPR, surface plasmon resonance; TEM, transmission electron microscopy.

homodimers that organize themselves into a triangular ring. In fact, the isolated NTD of *Mycobacterium tuberculosis* DnaB has also been observed to form a trimer-of-dimers arrangement (PDB ID 2R5U) [10]. Additionally, the NTD ring has been shown to be important for helicase motility activity and for binding specific partner proteins [11–13]. In contrast, CTDs interact with each other according to a circular ring with a hexameric symmetry and present the ATPase activity and DNA interaction surfaces [8,13–15].

Structure determinations of DnaB complexed with ATP, ATPγS, AMP-PNP, ADP, ssDNA or protein partners, have revealed multiple quaternary structure arrangements (see [16] for a review) [17,18]. For instance, the crystal structure of the *Geobacillus stearothermophilus apo*-DnaB that, when complexed with a domain of DnaG, showed a flat, two-tier configuration with the NTD "collar" forming a trimer of dimers, and the CTD ring with an exact or approximate threefold symmetry (PDB ID 2R6E and 2R6D, respectively) [13]. No nucleotide was bound to the DnaB hexamer, which formed a ~ 50 Å dilated channel, wide enough to accommodate dsDNA. In contrast, the helicase from *Aquifex aeolicus* in complex with ADP showed a constricted sixfold symmetry arrangement of the CTDs and a highly constricted triskelion arrangement of the NTDs (PDB ID 4NMN) [6]. In the study of the crystal structure of *G. stearothermophilus* DnaB with ssDNA and GDP:AlF_4, a spiral arrangement of subunits around ssDNA was revealed, suggesting a hand-over-hand translocation mechanism in which sequential hydrolysis of NTP is coupled with two nucleotide translocation steps along ssDNA (PDB ID 4ESV) [19]. Additionally, in a recent study, it was found that the helical hexamer loader DnaC from *Escherichia coli*, bound to ADP:BeF_3, cracks open the *Ec*DnaB ring in a DNA loading-competent structure (PDB ID 6QEL) [20].

The numerous available 3D structures of DnaB provide valuable but still incomplete insight into the complex interplay between structural states and helicase function. In particular, the significance of the dilated planar DnaB structures remains unclear. We present here the crystal structure of the *apo*-DnaB from *Vibrio cholerae*, which forms a novel *pseudo*-symmetric hexamer structure, constituted by a trimer of dimers organized in a dilated and planar shape, in which the CTD ring delimits a triskelion-shaped hole. Our findings show that this helicase conformation is inactive and labile and may constitute an intermediate state from dimers to active nucleotide-bound hexameric rings.

Materials and methods

Protein sample preparation

*Vc*DnaB was produced and purified as described in [15]. The buffers used for the first two purification steps (Ni-NTA and Superdex 200) were supplemented with ATP 1 mM and $MgCl_2$ 3 mM. The last MonoQ chromatography step was performed without ATP+Mg^{2+}. The pure protein sample was concentrated up to 24 mg·mL^{-1}, aliquoted, and flash-frozen in liquid nitrogen for storage at −80 °C.

ATPase activity

ATPase activity was assayed by linking ATP hydrolysis to the oxidation of NADH as described in [21]. The ATPase reaction was measured as a function of time at 340 nm by a GS08-Fluorimeter (Tecan, Männedorf, Switzerland), at 37 °C in a buffer containing Tris–HCl 50 mM (pH 7.5), NaCl 150 mM, and $MgCl_2$ 5 mM.

DNA binding measurement by surface plasmon resonance analysis

Surface plasmon resonance (SPR) was measured using a Proteon XPR36 instrument (Bio-Rad, Hercules, CA, USA). The measurements were performed at 30 °C in a PBS buffer (Bio-Rad) complemented with 0.01% of Tween 20 (PBST) and with or without ATP 0.5 mM (and without $MgCl_2$). NLC sensor chips (Bio-Rad) were used to immobilize the 50-mer oligonucleotide Oso15 described in [15], through its 3′ biotin-tag. For immobilization, DNA was diluted in PBST and attached to the NLS sensor chip (Bio-Rad) to obtain 50 RU. For the observation of kinetic data, *Vc*DnaB was injected at 50 µL·min^{-1} in PBST with or without 0.5 mM ATP during 240 s, and dissociation was run during 900 s in the same buffer. *Vc*DnaB was injected at different concentrations, from 0.312 to 5 µM. After each interaction test, the chip was regenerated using 0.5% of SDS. After correcting by subtraction of the uncoated reference channel, the sensorgrams were analyzed and compared.

Crystal structure determination of *apo-Vc*DnaB

Native protein crystals were grown in 100 nL sitting drops distributed automatically by the Mosquito pipetting robot, by mixing *Vc*DnaB (at a concentration of 0.115 mM of monomer) with a reservoir solution in a 1 : 1 ratio. Unexpectedly, despite the fact that *Vc*DciA and GDP were present in the initial protein mixture (0.115 mM *Vc*DciA + 2 mM GDP + 5 mM NaF + 0.5 mM $AlCl_3$ + 3 mM $MgCl_2$), crystals of *apo-Vc*DnaB alone were obtained. Numerous small cubic crystals of *apo-Vc*DnaB

appeared after 3 days at 18 °C in 0.1 M sodium acetate (pH4.6) + 1.2 M sodium malonate. Glycerol cryo-protected crystals (one-step at 30% glycerol) were flash-frozen in liquid nitrogen. Diffraction data and refinement statistics are given in Table 1. Crystallographic data were collected at the PROXIMA-1 beamline from Synchrotron SOLEIL (Saint-Aubin, France) and processed with XDS [22] through XDSME [23]. Diffraction anisotropy was corrected using the STARANISO server (http://staraniso.globalphasing.org). The *Vc*DnaB crystal structure was solved by molecular replacement with the MOLREP program [24] using the X-ray structure of the DnaB·GDP:AlF_4:Mg^{2+} from *V. cholerae* (GDP-bound structure, PDB ID 6T66) [15]. The model refinement was conducted with the BUSTER program using TLS and strong non-crystallographic symmetry restraints [25] keeping the CTD and NTD separated. The model was corrected and completed using COOT [26].

Table 1. X-ray statistics.

	*apo-Vc*DnaB[a]
Data collection[b]	
Space group	$P2_12_12_1$
Cell dimensions	
a, *b*, *c* (Å)	141.2, 150.1, 188.3
α, β, γ (°)	90.0, 90.0, 90.0
Resolution range (Å)	50–3.8 (3.9–3.8)
Before STARANISO	
Completeness (%)	99.9 (99.9)
$I/\sigma(I)$	5.1 (0.3)
After STARANISO	
Completeness (%)	72.4 (13.1)
$I/\sigma(I)$	6.9 (1.0)
R_{merge} (%)	30.6 (308.8)
R_{pim} (%)	8.9 (86.6)
Redundancy	13.6 (13.5)
CC(1/2)	0.996 (0.527)
Refinement	
Resolution range (Å)	32.6–3.8
No. reflections work set/test set	29,095/1408
R/R_{free} (Buster, %)	26.5/27.4
No. atoms	
Protein	20,679
Ligand/ion	0
Water	0
R.m.s. deviation bonds (Å)	0.004
R.m.s. deviation angles (°)	0.61
Average B-factor (Å^2)	
From atoms	178.0
From Wilson plot	113.3
Ramachandran plot	
Most favored (%)	94.2
Outliers (%)	0.11
Molprobity score	2.17

[a]Diffraction data collected from one crystal, which diffracted anisotropically to 4.2 Å along *a**, 3.6 Å along *b** and 4.7 Å along *c**.; [b]Values in parentheses refer to the highest resolution shell.

Small-angle X-ray scattering

The small-angle X-ray scattering (SAXS) experiment was performed on the SWING beamline at the synchrotron SOLEIL (Saint-Aubin, France) as described in [15]. The data were collected after elution of the protein through the online size-exclusion high-performance liquid chromatography column (Superose 6 Increase 10/300 GL; GE Healthcare, Chicago, IL, US) equilibrated in Tris–HCl 20 mM (pH 8.8), NaCl 100 mM. The scattered intensities were displayed on an absolute scale using the scattering by water. For each frame, the protein concentration (below 1 mg·mL^{-1} at the top of elution peak) was estimated from UV absorption at 280 nm using a spectrophotometer located immediately upstream of the SAXS measuring cell. Data were first analyzed using Foxtrot, the SWING in-house software, and then using the US-SOMO HPLC module [27]. This program provided for each SAXS frame the values of the scattering intensity $I(0)$ and of the radius of gyration Rg by applying the Guinier analysis together with a calculation of the approximate molar mass using the Rambo and Tainer approach [28].

Transmission electron microscopy (TEM)

The *Vc*DnaB protein at a concentration of 24 mg·mL^{-1} (0.45 mM for the monomer) in Tris–HCl 20 mM (pH 8.8), NaCl 200 mM and stored at −80 °C, was thawed on ice and diluted in the same buffer in the absence or in the presence of ADP 1 mM and $MgCl_2$ 3 mM. A direct dilution of factor 200 was made in the presence (Sample 1) or in the absence (Sample 2) of ADP+$MgCl_2$. Two consecutive twofold dilutions were then applied in a buffer lacking ADP+$MgCl_2$. Samples were analyzed by conventional electron microscopy using the negative staining method. Three microliters of sample suspension were deposited on an air glow-discharged 400 mesh copper carbon-coated grid for 1 min. The excess liquid was blotted, and the grid rinsed with 2% w/v aqueous uranyl acetate. The grids were visualized at 100 kV with a Tecnai 12 Spirit transmission electron microscope (Thermo Fisher, New York, NY, USA) equipped with a K2 Base 4 k × 4 k camera (Gatan, Pleasanton, CA, USA), on the I2BC cryo-electron microscopy facility (Gif-sur-Yvette, France). Nominal magnification was at 26 000×, corresponding to a pixel size at the level of the specimen of 0.18 nm. A general observation was made by counting identifiable ring-shaped particles per micrograph.

Results and Discussion

*apo-Vc*DnaB crystallizes as a planar ring-shaped trimer of dimers

Escherichia coli recombinant expression of *Vc*DnaB in the presence of chaperone proteins [15,29] yielded

about 10 mg of protein per liter of culture. The purification process used standard protocols, combining Ni-NTA and gel filtration but in the presence of ATP+Mg^{2+} in the purification buffers. We noted that this procedure was necessary to isolate a fully active helicase for translocation [15]. The final MonoQ ion-exchange purification step was carried out without ATP+Mg^{2+}.

Although *Vc*DciA and GDP:AlF_4+Mg^{2+} were present in the crystallization mixture, *Vc*DnaB was the only molecule to crystallize and formed small cubic crystals diffracting anisotropically up to 3.8 Å resolution. The data collection parameters and refinement statistics are listed in Table 1. We observed that six copies of *Vc*DnaB were present in the asymmetric unit. Each is composed of the canonical NTD and CTD domains of the DnaB helicases, connected by the linker described as the LH (linker helix) in the GDP-bound *Vc*DnaB structure [15] (Fig. 1). Each of the two domains is present in six similar copies and does not show significant variation with both of two NTD and CTD domains of the GDP-bound *Vc*DnaB structure (PDB ID 6T66, RMSD of 1.4 and 1.8 Å, respectively, for the NTD and the CTD domains).

We observed that the *apo*-*Vc*DnaB helicase adopts the typical quaternary structure with the two ring layers to be present (top of Fig. 1). The threefold symmetry of the triangular NTD face, as present in many other structures such as GDP-bound *Vc*DnaB [15] or *apo*-*Gst*DnaB [13], is maintained and creates a ~ 50 Å wide channel (Figs 1 left and 2A) [6]. In contrast, the hexameric symmetry of the CTD face observed in the GDP-bound *Vc*DnaB structure [15] was broken to form a trimer of dimers with a threefold symmetry

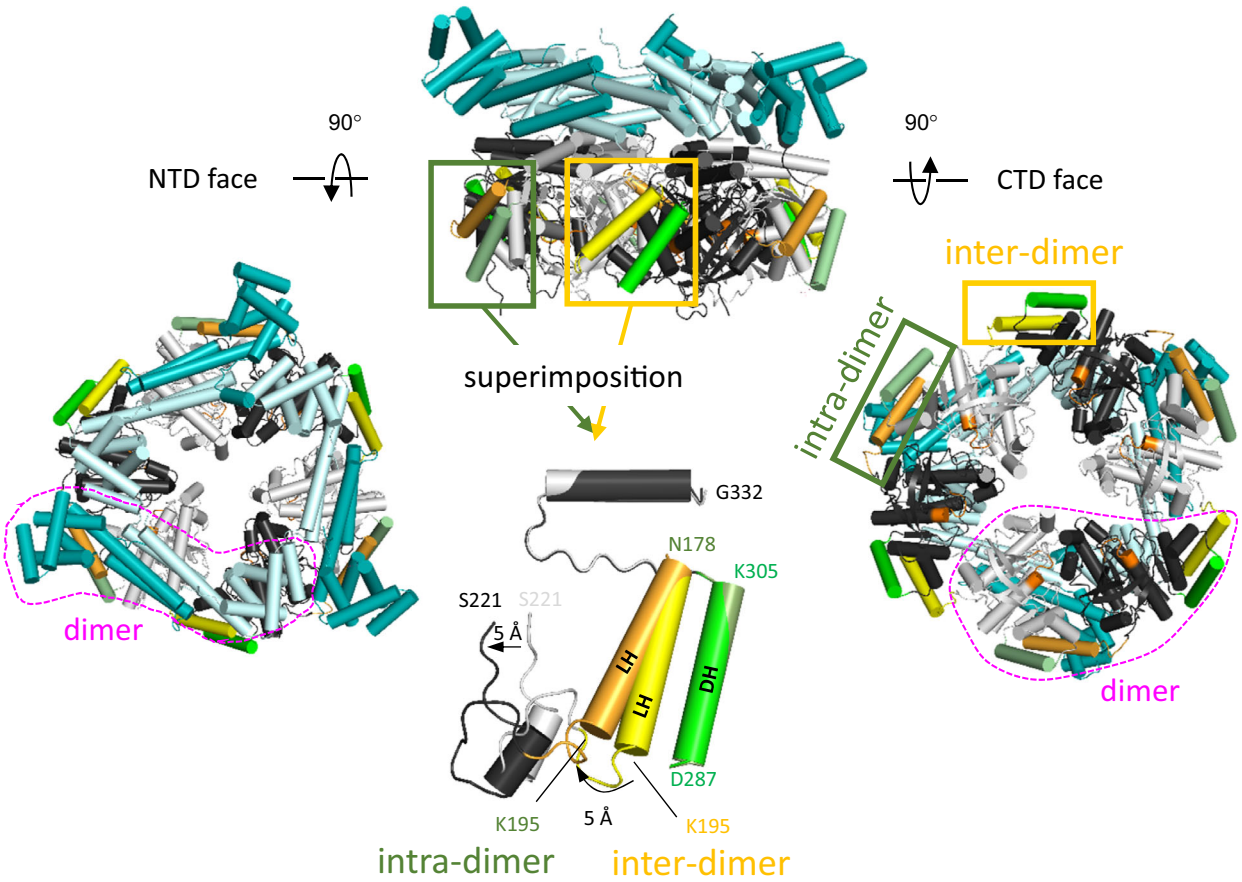

Fig. 1. Crystal structure of the *apo*-*Vc*DnaB. The NTD face (in two shades of blue, left), side (top) and CTD face (in two shades of gray, right) views of *apo*-*Vc*DnaB are presented. The LH helix (linker between the NTD and CTD domains) and the DH helix (which contains the determinant serine residue of *Vc*DnaB [15]) are in two shades of yellow and green, respectively. The yellow and orange frames indicate the regions of the inter- and intra-dimeric LH-DH modules, respectively, that are compared: The DH helices plus their next helices (residues D287 to G332) are superimposed, showing the 5 Å shift of the LH helix (zoom at the bottom). The pink lines surround the NTD (left) and CTD (right) dimers. The 6 P-loops of the Walker A ^{228}ARPSMGKT^{235} signature are in orange (CTD face, right).

FEBS Letters **596** (2022) 2031–2040 © 2022 The Authors. FEBS Letters published by John Wiley & Sons Ltd on behalf of Federation of European Biochemical Societies.

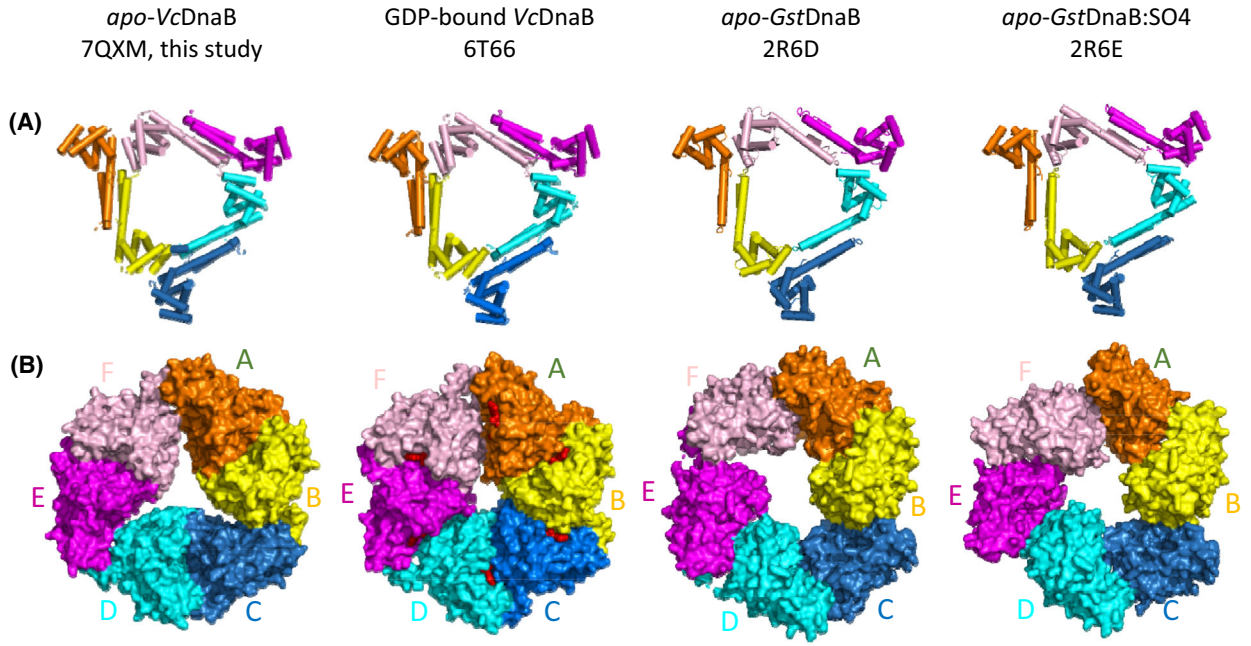

Fig. 2. Quaternary assemblies of the replicative helicase NTD and CTD rings according to nucleotide-binding and to bacterial species. The three dimers of the *apo*-*Vc*DnaB (PDB ID 7QXM, this study), of the GDP-bound *Vc*DnaB (PDB ID 6T66, [15]) and of the *apo*-*Gst*DnaB (PDB ID 2R6D and 2R6E, [13]) are colored in orange + yellow (A and B subunits), blue and cyan (C and D subunits), and magenta + light pink (E and F subunits). (A) Global organization of the NTD rings. The classical threefold symmetry triangular conformation with an open channel of ~ 50 Å in diameter is maintained for the NTDs in the 4 structures. (B) Global organization of the CTD rings. The dilated triskelion-shaped hole of the *apo*-*Vc*DnaB CTD *pseudo*-hexamer (left) contrasts with the constricted hole of the GDP-bound *Vc*DnaB typical CTD hexamer (middle left) and with the distorted hole of the irregular CTD ring of *apo*-*Gst*DnaB crystal form B1 (PDB ID 2R6D, middle right), but it presents a threefold symmetry more similar to the CTD trimer of dimers of *apo*-*Gst*DnaB crystal form B2 (PDB ID 2R6E, right).

(Figs 1 right and 2B left and middle left). The CTD ring of *apo*-*Vc*DnaB creates a dilated and triskelion-shaped hole (Fig. 2B left), which differs from the constricted round hole observed in the GDP-bound complex (Fig. 2B middle left) [15]. As for the CTD rings of the *apo*-*Gst*DnaB structures, they form a very dilated hexamer either irregular with no rotational symmetry or with a threefold symmetry approaching that of *apo*-*Vc*DnaB [13] (Fig. 2B middle right and right, respectively). The loss of the strict sixfold symmetry of the hexameric CTD ring could be a specificity of the *apo*-forms of DnaB replicative helicases.

To examine the *apo*-*Vc*DnaB conformation closer, we measured the distance between each LH and its neighboring helix, named determinant helix (DH) [15], and compared the distances according to their belonging to the intra- or inter-dimer interfaces (bottom of Fig. 1). With this measurement, we noted that the LHs helices in the inter-dimer regions are closer to the DH helices than the intra-dimer LHs helices with a variation of about 5 Å (bottom of Fig. 1). This light slip of the dimers relative to each other allows the CTD ring to adopt this unusual *pseudo*-symmetric hexamer conformation and leads to the widening of the CTD ring hole with a triskelion shape in comparison with the constricted round hole of the GDP-bound *Vc*DnaB structure (Fig. 2B left and middle left, respectively). Another observation was the flattening of the ring of the *apo*-*Vc*DnaB hexamer, in contrast with the slightly spiral-open configuration of GDP-bound *Vc*DnaB [15]. The distances between the 6 LH-DH modules of the *apo* and GDP-bound forms are similar (top of Fig. 3), and their superimposition makes it possible to visualize this flattening (bottom of Fig. 3). The two CTD rings show a twisted shift of ~ 20 Å for the GDP-bound form relative to the planar *apo*-form (Fig. 3).

Although the regions involved in subunit contacts between the *apo* and GDP-bound forms are similar, there are significant differences in the number of polar interactions and buried interface areas. The three intra-dimer interface areas (Table 2) from the *apo*-structure are slightly larger (8% more) than those from GDP-bound *Vc*DnaB. A notable difference is observed for the buried surface areas at the inter-dimer interfaces

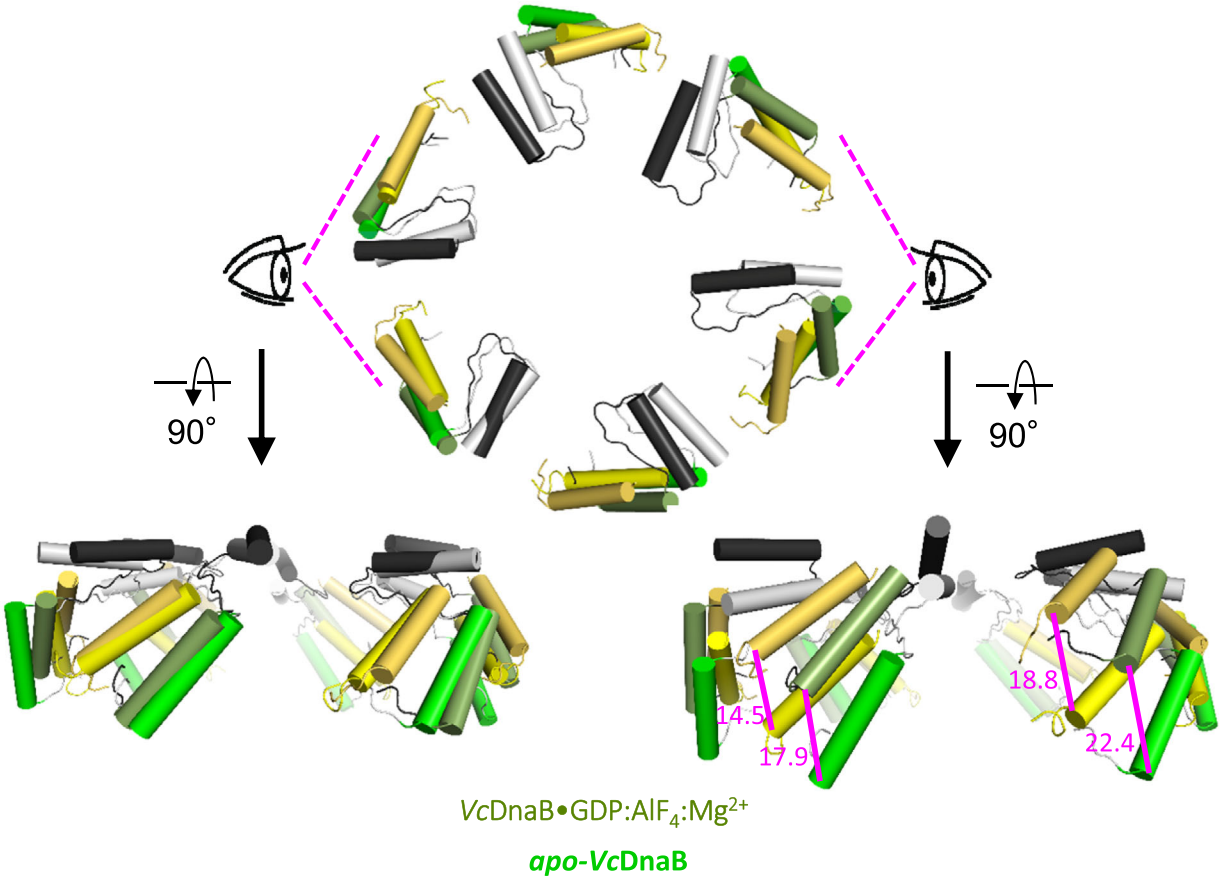

Fig. 3. *Pseudo*-symmetric hexamer of *apo-Vc*DnaB is planar. The superimposition of the six LH-DH modules (residues N178-G200 and T283-H331, colored as in Fig. 1) of the *apo-Vc*DnaB (PDB ID 7QXM, this study) and the GDP-bound *Vc*DnaB (PDB ID 6T66, [15]) shows that they are equidistant and similar between the two structures. However, the CTD ring of *apo-Vc*DnaB is closed and planar while that of the GDP-bound structure is slightly spiral-open as described in [15], which causes a maximum shift of about 20 Å between the LH-DH modules at the ring opening (bottom right).

between the two DnaB hexamers. While this surface area is the same for the three interfaces of the *apo*-form (average of 2101 Å^2), the buried surface differs considerably for the three inter-dimers of the GDP-bound form (between 1700 and 2500 Å^2). This is due to a slight opening of the ring in the GDP-bound form [15], which could be related to the ring breaking step during the loading of the helicase onto the DNA [20]. Another notable difference is also observed in the distribution of subunit contacts of the *apo* and GDP-bound forms. While the number of chemical bonds is equivalent in the two types of interfaces of the *bona fide* hexameric GDP-bound structure, the number of these interactions in the *apo-Vc*DnaB is much lower in the inter-dimer interfaces than in the intra-dimer interfaces (average of 14.3 H-bonds and 11.3 salt bridges to be compared with average of 24.3 and 15.6, respectively, Table 2). It is, therefore, expected that the two hexamers will have a different stability: the *pseudo*-hexamer of *apo-Vc*DnaB could dissociate more easily into dimers.

The *apo-pseudo*-hexamer ring of *Vc*DnaB is inactive and labile

The first two purification steps of the *apo-Vc*DnaB were performed in the presence of ATP+Mg^{2+}. To ensure that we finally removed ATP+Mg^{2+} of our purified helicase, we measured the residual ATPase activity of the protein sample (Fig. 4A) and confirmed that our protein sample was only marginally occupied by nucleotides. This was further confirmed by the absence of bound nucleotide in the crystal structure. The ^{228}ARPSMGKT^{235} Walker A motif conformations are similar between the *apo* and the GDP-bound forms (Fig. 4B). The maximum difference between two Cα

Table 2. Subunit interface contacts[a].

	*apo-Vc*DnaB (this study)			GDP-bound *Vc*DnaB (PDB ID 6T66)		
	Interface area Å^2	#H-bonds	#Salt bridges	Interface area Å^2	#H-bonds	#Salt bridges
Intra-dimers						
AB	3647	27	17	3405	20	17
CD	3648	24	18	3300	18	13
EF	3536	22	12	3276	17	11
Inter-dimers						
BC	2170	16	14	2508	20	18
DE	2182	15	11	1666	16	8
FA	1952	12	9	1805	19	11

[a]The data have been generated using the PISA server [30].

atoms in the two superimposed P-loops is 2.2 Å, probably due to the absence or presence of phosphate ligand in *apo* and GDP-bound *Vc*DnaB structures, respectively. This is consistent with our observation that the *apo*-form is not a dead-end amorphous state, since when ATP was added, its hydrolysis was measured (Fig. 4A). We propose that the *apo-Vc*DnaB structure could be an intermediate conformation toward the nucleotide-bound hexameric active state.

Using SPR, we measured the influence of ATP on the *Vc*DnaB binding onto DNA (Fig. 4C). The ssDNA fixed to the chip presents a 5′ extremity accessible for the helicase. As we previously demonstrated that in the presence of ATP *Vc*DnaB remains strongly bound to the DNA [15], we reproduced this experiment and confirmed this observation (Fig. 4C, pink to brown curves). The association is dependent on protein concentrations, and the dissociation is very slow. On the contrary, in the absence of ATP, we did not observe binding of the helicase to DNA (Fig. 4C, blue to black curves), showing that ATP is required for this interaction.

SAXS analyses coupled with size-exclusion chromatography of *apo-Vc*DnaB showed that the average molar mass of the scattering object decreased continuously during the elution of the protein (red line in Fig. 5A). This suggests the presence of oligomers, varying from dodecamers to dimers, showing the instability of the hexamers. We previously observed that nucleotide-bound *Vc*DnaB is predominantly hexameric and remains stable during gel filtration [15]. We conclude that the hexameric form of *apo-Vc*DnaB is less stable than that of the nucleotide-bound form, as suspected by the X-ray structures analysis presented above (Table 2).

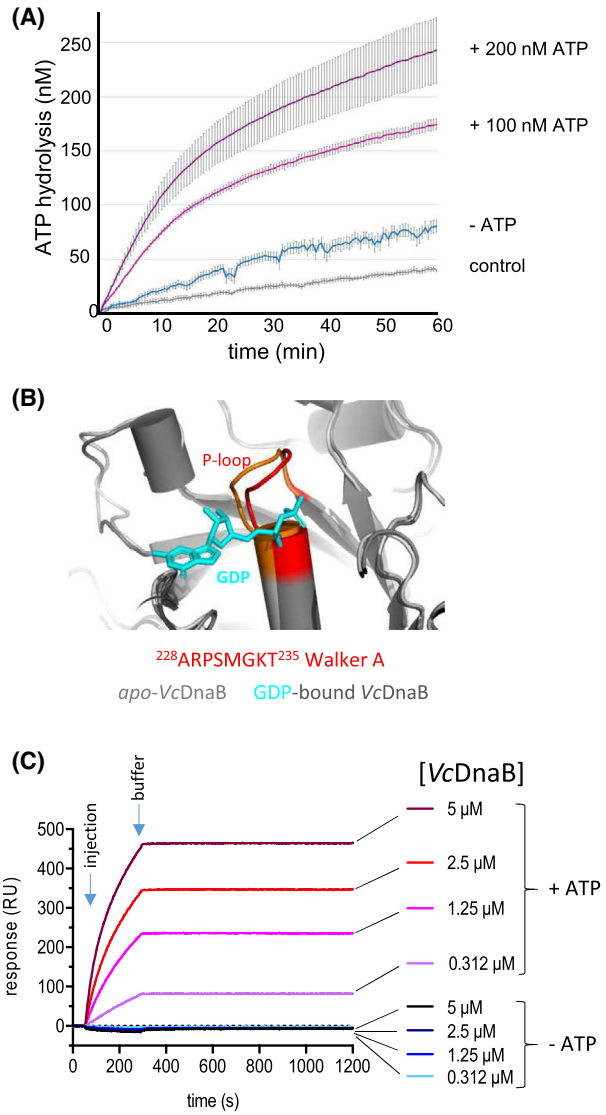

Fig. 4. *apo-Vc*DnaB is inactive. (A) The purified *Vc*DnaB sample has a low residual ATPase activity. The ATP hydrolysis measurements were done in triplicate with 125 nM of *Vc*DnaB, without adding ATP in the reaction mixture (blue line) or with 100 and 200 nM ATP added (pink and purple curves, respectively). (B) The empty ATP-binding pocket of *apo-Vc*DnaB subunit A (in light gray, PDB 7QXM, this study) is superimposed with the equivalent pocket of GDP-bound *Vc*DnaB subunit A (in dark gray, PDB ID 6T66, [15]). GDP is in cyan sticks. The two P-loops are in orange and red, respectively, for the *apo*- and the GDP-bound *Vc*DnaB. The maximum distance deviation between the two P-loops is of 2.2 Å. (C) ssDNA interaction analysis by SPR. The single-stranded DNA oligonucleotide was bound to the SPR matrix through its 3′ biotinylated extremity, leaving a 5′ end accessible. *Vc*DnaB was injected at the indicated concentrations (from 0.312 to 5 µM), with ATP 0.5 mM (from light pink to brown curves) or without ATP (from light blue to black curves). ATP is required for *Vc*DnaB to bind ssDNA.

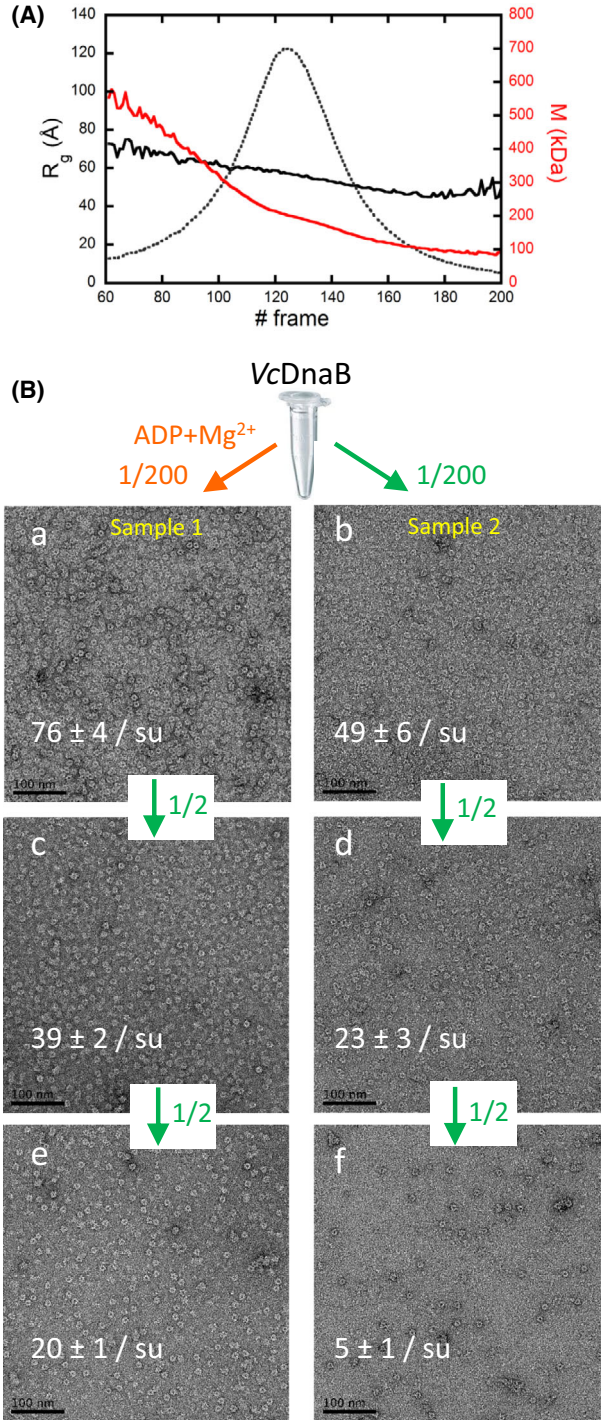

Fig. 5. *apo-Vc*DnaB ring is unstable. (A) The structural analysis of *Vc*DnaB in solution was carried out by SAXS without ATP, showing the evolution of the radius of gyration Rg (thick black curve) and the molar mass (red curve) as a function of the SEC-SAXS elution profile. The forward scattered intensity *I*(0) (thin dashed black curve) is also represented. The average molar mass of the scattering object decreased continuously during the elution of *apo-Vc*DnaB, suggesting the presence of oligomers of various sizes, ranging from dodecamers to dimers. (B) Negative staining electron microscopy was performed on *Vc*DnaB, after a 1/200 dilution in the presence (panel a) or in the absence (panel b) of ADP+Mg^{2+}. In the presence of ADP, the grid was covered with rings (panel a) whose number was halved, for each of the two successive 1/2 dilutions applied (panels c and e). In the absence of ADP, the first dilution by 200 resulted in visible rings with aggregates (panel b). Ring-shaped particles were visible in the subsequent 1/2 dilution (panel d), but their number dropped by a factor of 5 following the last 1/2 dilution (panel f). The black scale bars represent a 100 nm distance on these representative electron micrographs. The surface unit (su) corresponds to 1/9 of a micrograph. The counting of the rings was done in 3 su, which were averaged.

TEM analysis of *Vc*DnaB pre-incubated with ADP+Mg^{2+} (Sample 1), as described in [15], showed a homogenous and numerous ring-shaped species population (particles/surface unit = 76 ± 4, Fig. 5Ba). On the contrary, when ADP+Mg^{2+} was omitted in the dilution buffer (Sample 2), *Vc*DnaB adopted in majority a ring shape structure but a larger amount of aggregates is also visible (p/su = 49 ± 6, Fig. 5Bb). Next, the two samples were twofold diluted consecutively with buffer lacking ADP+Mg^{2+}, and each dilution step was analyzed on grids. For Sample 1, the rate of hexameric structures decreased proportionally (p/su = 39 ± 2 and p/su = 20 ± 1, Fig. 5Bc, Be), indicating that the nucleotide-bound hexamer is stable. The first twofold dilution step of Sample 2 resulted in a smaller number of rings compared with Fig. 5Bc (p/su = 23 ± 3, Fig. 5Bd). The second step of the twofold dilution of Sample 2 did not yield a proportional number of rings, falling from 23 ± 3 to 5 ± 1 particles per unit surface, which corresponds to a ratio of 1/5 (Fig. 5Bf). The light and granular background of this grid (Fig. 5Bf) also suggests the presence of proteins, not organized in hexamers but probably with a lower degree of oligomerization. Using TEM, we confirmed the lability of the *apo*-hexamer observed by SAXS. We, therefore, propose that the organization and the maintenance of the active form of *Vc*DnaB are dependent on the presence of a nucleotide.

Conclusion

Here, we described the crystal structure of *apo*-DnaB from *V. cholerae*, composed of the typical triangular threefold symmetry NTD face and a novel threefold symmetry CTD ring, which delimits a dilated triskelion-shaped hole. This contrasts with the GDP-bound *Vc*DnaB that forms the typical sixfold symmetry CTD ring, with a constricted round hole. We propose that the structure of *apo-Vc*DnaB could reflect an

FEBS Letters **596** (2022) 2031–2040 © 2022 The Authors. FEBS Letters published by John Wiley & Sons Ltd on behalf of Federation of European Biochemical Societies.

intermediate and inactive state from the association of dimers to the hexamerization process of the helicase. It should be noted that because of the abundant omnipresence of ATP in the cell, it is unlikely that the labile *apo-Vc*DnaB forms persist *in vivo* and *Vc*DnaB should be rapidly assembled into active nucleotide-bound hexameric rings.

Acknowledgements

X-ray diffraction and SAXS data were collected at Synchrotron SOLEIL (Saint-Aubin, France; beamlines PROXIMA-1 and SWING, respectively). We thank the beamlines staff and Ines Li de la Sierra-Gallay for assistance and advice during data collection. This work benefited from the CryoEM and the PIM platforms of I2BC (Gif-sur-Yvette, France), supported by the French Infrastructure for Integrated Structural Biology (FRISBI) (ANR-10-INSB-05-05). We are grateful to Melissa-Ann Thomas from the Academic Writing Center (Université Paris-Saclay) and to Herman van Tilbeurgh for proofreading the text.

Author contributions

SM, J-LF, and SQ-C conceived this study; CC purified and crystallized the proteins; SM and CC performed the SPR and biochemical assays; HW, CC, and PL performed the X-ray structure determinations and refinements; CC and MOA performed the electron microscopy experiments; DD and SQ-C performed the SEC-SAXS experiments; SQ-C, and HW wrote the paper with input from all authors.

Funding

This work was supported by the French Infrastructure for Integrated Structural Biology (FRISBI) ANR-10-INBS-05 and by funds from the Centre National de la Recherche Scientifique (CNRS). CC was supported by a PhD fellowship from the French Ministry of Education.

Data accessibility

The *apo-Vc*DnaB crystal structure reported in this paper is openly available in the wwPDB with the accession number 7QXM.

References

1 Lewis JS, Jergic S, Dixon NE. The *E. coli* DNA replication fork. *Enzymes*. 2016;**39**:31–88.
2 Monachino E, Jergic S, Lewis JS, Xu ZQ, Lo ATY, O'Shea VL, et al. A primase-induced conformational switch controls the stability of the bacterial replisome. *Mol Cell*. 2020;**79**:140–54.e7.
3 Xu ZQ, Dixon NE. Bacterial replisomes. *Curr Opin Struct Biol*. 2018;**53**:159–68.
4 Berger JM. SnapShot: nucleic acid helicases and translocases. *Cell*. 2008;**134**:888–888.e1.
5 Singleton MR, Dillingham MS, Wigley DB. Structure and mechanism of helicases and nucleic acid translocases. *Annu Rev Biochem*. 2007;**76**: 23–50.
6 Strycharska MS, Arias-Palomo E, Lyubimov AY, Erzberger JP, O'Shea VL, Bustamante CJ, et al. Nucleotide and partner-protein control of bacterial replicative helicase structure and function. *Mol Cell*. 2013;**52**:844–54.
7 Bailey S, Eliason WK, Steitz TA. The crystal structure of the *Thermus aquaticus* DnaB helicase monomer. *Nucleic Acids Res*. 2007;**35**:4728–36.
8 Lo YH, Tsai KL, Sun YJ, Chen WT, Huang CY, Hsiao CD. The crystal structure of a replicative hexameric helicase DnaC and its complex with single-stranded DNA. *Nucleic Acids Res*. 2009;**37**:804–14.
9 Ye J, Osborne AR, Groll M, Rapoport TA. RecA-like motor ATPases–lessons from structures. *Biochim Biophys Acta*. 2004;**1659**:1–18.
10 Biswas T, Tsodikov OV. Hexameric ring structure of the N-terminal domain of *Mycobacterium tuberculosis* DnaB helicase. *FEBS J*. 2008;**275**:3064–71.
11 Fass D, Bogden CE, Berger JM. Crystal structure of the N-terminal domain of the DnaB hexameric helicase. *Structure*. 1999;**7**:691–8.
12 Weigelt J, Brown SE, Miles CS, Dixon NE, Otting G. NMR structure of the N-terminal domain of *E. coli* DnaB helicase: implications for structure rearrangements in the helicase hexamer. *Structure*. 1999;**7**:681–90.
13 Bailey S, Eliason WK, Steitz TA. Structure of hexameric DnaB helicase and its complex with a domain of DnaG primase. *Science*. 2007;**318**: 459–63.
14 Barcena M, Ruiz T, Donate LE, Brown SE, Dixon NE, Radermacher M, et al. The DnaB.DnaC complex: a structure based on dimers assembled around an occluded channel. *EMBO J*. 2001; **20**:1462–8.
15 Marsin S, Adam Y, Cargemel C, Andreani J, Baconnais S, Legrand P, et al. Study of the DnaB:DciA interplay reveals insights into the primary mode of loading of the bacterial replicative helicase. *Nucleic Acids Res*. 2021;**49**:6569–86.
16 Oakley AJ. A structural view of bacterial DNA replication. *Protein Sci*. 2019;**28**:990–1004.

17 Yu X, Jezewska MJ, Bujalowski W, Egelman EH. The hexameric *E. coli* DnaB helicase can exist in different quaternary states. *J Mol Biol*. 1996;**259**:7–14.
18 San Martin C, Radermacher M, Wolpensinger B, Engel A, Miles CS, Dixon NE, et al. Three-dimensional reconstructions from cryoelectron microscopy images reveal an intimate complex between helicase DnaB and its loading partner DnaC. *Structure*. 1998;**6**:501–9.
19 Itsathitphaisarn O, Wing RA, Eliason WK, Wang J, Steitz TA. The hexameric helicase DnaB adopts a nonplanar conformation during translocation. *Cell*. 2012;**151**:267–77.
20 Arias-Palomo E, Puri N, O'Shea Murray VL, Yan Q, Berger JM. Physical basis for the loading of a bacterial replicative helicase onto DNA. *Mol Cell*. 2019;**74**:173–84.e4.
21 Pullman ME, Penefsky HS, Datta A, Racker E. Partial resolution of the enzymes catalyzing oxidative phosphorylation. I. Purification and properties of soluble dinitrophenol-stimulated adenosine triphosphatase. *J Biol Chem*. 1960;**235**:3322–9.
22 Kabsch W. XDS. *Acta Crystallogr D Biol Crystallogr*. 2010;**66**:125–32.
23 Legrand, P. (2017) XDSME: XDS made easier *GitHub repository*. https://githubcom/legrandp/xdsme. Accessed 1 Aug 2017.
24 Vagin A, Teplyakov A. Molecular replacement with MOLREP. *Acta Crystallogr D Biol Crystallogr*. 2010;**66**:22–5.
25 Smart OS, Womack TO, Flensburg C, Keller P, Paciorek W, Sharff A, et al. Exploiting structure similarity in refinement: automated NCS and target-structure restraints in BUSTER. *Acta Crystallogr D Biol Crystallogr*. 2012;**68**:368–80.
26 Emsley P, Lohkamp B, Scott WG, Cowtan K. Features and development of Coot. *Acta Crystallogr D Biol Crystallogr*. 2010;**66**:486–501.
27 Brookes E, Vachette P, Rocco M, Perez J. US-SOMO HPLC-SAXS module: dealing with capillary fouling and extraction of pure component patterns from poorly resolved SEC-SAXS data. *J Appl Cryst*. 2016;**49**:1827–41.
28 Rambo RP, Tainer JA. Accurate assessment of mass, models and resolution by small-angle scattering. *Nature*. 2013;**496**:477–81.
29 Nishihara K, Kanemori M, Kitagawa M, Yanagi H, Yura T. Chaperone coexpression plasmids: differential and synergistic roles of DnaK-DnaJ-GrpE and GroEL-GroES in assisting folding of an allergen of Japanese cedar pollen, Cryj2, in *Escherichia coli*. *Appl Environ Microbiol*. 1998;**64**:1694–9.
30 Krissinel E, Henrick K. Inference of macromolecular assemblies from crystalline state. *J Mol Biol*. 2007;**372**:774–97.